BioMedical Engineering OnLine

RESEARCH

Open Access

A finger on the pulse of cardiovascular health: estimating blood pressure with smartphone photoplethysmography-based pulse waveform analysis

Ivan Shih-Chun Liu[1,2], Fangyuan Liu[1], Qi Zhong[2] and Shiguang Ni[3,4*]

*Correspondence:
ni.shiguang@sz.tsinghua.edu.cn

[1] Department of Psychology, Faculty of Arts and Sciences, Beijing Normal University at Zhuhai, Zhuhai, Guangdong, China
[2] Faculty of Psychology, Beijing Normal University, Beijing, China
[3] Shenzhen International Graduate School, Tsinghua University, Shenzhen, China
[4] University Town of Shenzhen, Nanshan District, Shenzhen 518055, China

Abstract

Smartphone photoplethysmography (PPG) offers a cost-effective and accessible method for continuous blood pressure (BP) monitoring, but faces persistent challenges with accuracy and interpretability. This study addresses these limitations through a series of strategies. Data quality was enhanced to improve the performance of traditional statistical models, while SHapley Additive exPlanations (SHAP) analysis ensured transparency in machine learning models. Waveform features were analyzed to establish theoretical connections with BP measures, and feature engineering techniques were applied to enhance prediction accuracy and model interpretability. Bland–Altman analysis was conducted, and the results were compared against reference devices using multiple international standards to evaluate the method's feasibility. Data collected from 127 participants demonstrated strong correlations between smartphone-derived digital waveform features and those from reference BP devices. The mean absolute errors (MAE) for systolic BP (SBP), diastolic BP (DBP), and pulse pressure (PP) using multiple linear regression models were 7.75, 6.35, and 4.49 mmHg, respectively. Random forest models further improved these values to 7.34, 5.79, and 4.45 mmHg. Feature importance analysis identified key contributions from time-domain, frequency-domain, curvature-domain, and demographic features. However, Bland–Altman analysis revealed systematic biases, and the models barely meet established accuracy standards. These findings suggest that while smartphone PPG technology shows promise, significant advancements are required before it can replace traditional BP measurement devices.

Keywords: Smartphone photoplethysmography, Pulse waveform, Blood pressure, Interpretable machine learning, Explainable machine learning, SHapley Additive exPlanations (SHAP)

Introduction

The circulatory system is essential for delivering oxygen and nutrients to tissues while removing waste, making a balanced blood pressure (BP) critical for maintaining physiological homeostasis. Elevated BP is strongly associated with severe health conditions,

including heart attacks, strokes, kidney disease, and eye complications [37]. Routine BP monitoring is vital for early detection and management of these conditions. However, BP readings can vary significantly due to factors such as time of day, physical activity, dietary habits, and mental state [73]. Additionally, BP values can exhibit substantial variability between individual heartbeats [24], necessitating multiple measurements throughout the day for accurate assessment.

Despite its importance, continuous BP monitoring faces practical challenges. Access to medical-grade equipment is often limited [2], and portable devices can be inconvenient for daily use. Furthermore, sphygmomanometer-based devices may cause discomfort and temporarily disrupt blood flow during measurements [61]. To overcome these limitations, researchers have turned to optical technologies for continuous BP monitoring. These approaches range from oximeters specifically designed to monitor blood flow to camera-based methods that utilize general-purpose equipment for detecting blood volume changes [66, 74]. Among these, smartphone camera-based methods have gained considerable attention due to their accessibility compared to specialized devices and their superior accuracy relative to contactless camera-based approaches.

Smartphones equipped with built-in sensors offer two principal methods for BP estimation [21]. The first method, pulse arrival time (PAT), calculates the speed of the pressure wave generated by each heartbeat. However, this method requires an electrocardiogram (ECG) to detect pulse onset, limiting its practicality [70]. Although efforts have been made to estimate PAT using a single smartphone, this approach still relies on additional devices and lacks widespread adoption [59, 81, 91].

The second method, pulse waveform analysis (PWA), estimates BP by analyzing the shape of the pulse waveform (Figure 1). Arterial stiffness, commonly linked to elevated BP, accelerates the arrival of reflected waves within blood vessels, thereby altering the waveform's shape and amplitude [3]. A commonly employed technique for detecting blood flow waveforms is photoplethysmography (PPG), an optical method that measures blood volume changes beneath the skin caused by heartbeats [19]. By analyzing variations in light intensity, PPG calculates differences in hemoglobin absorption, enabling the assessment of blood volume increases during systole and decreases during diastole.

Traditionally, PPG signals have been acquired using finger oximeters with LED light sources [36]. These LED-based PPG methods have demonstrated reliable accuracy for BP estimation [72]. However, these approaches still require users to carry additional devices, which limits their practicality for everyday use. Recent advancements

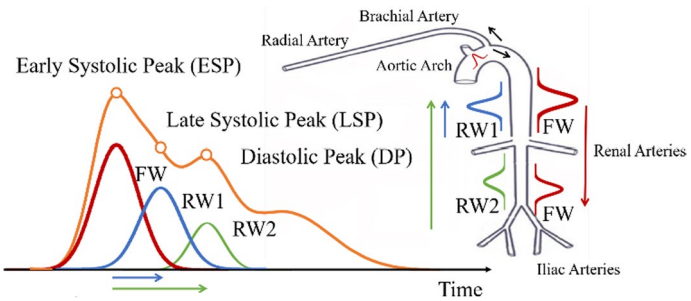

Fig. 1 The reflected waves and the shape of the digital arterial pulse waveform (adapted from [3])

have shifted attention to camera-based PPG methods, which detect heartbeats by recording skin color changes induced by blood flow and converting these changes into waveforms. This technique allows for remote PPG monitoring using webcams or surveillance cameras for non-contact heartbeat detection [43]. However, the inherent noise in non-contact methods significantly compromises accuracy, limiting their practical applicability. Consequently, smartphone-based PPG has emerged as a more accessible and viable alternative. This method involves placing a finger on the smartphone camera to measure blood volume changes through color variations in the fingertip skin, offering the convenience of widely available devices alongside the potential for continuous BP monitoring.

Despite its potential, smartphone PPG-based waveform analysis for blood pressure prediction (SPW-BP) has received limited attention in both research and practical applications. A recent systematic review by Frey et al. [25] identified only 25 studies on smartphone PPG-based BP monitoring in the literature, with just 60% of them employing PWA methods.

Several factors might contribute to the limited focus on SPW-BP. First, concerns have been raised about the feasibility of using smartphones for BP estimation given the complex dynamics of peripheral vascular resistance and the inherently low signal quality of smartphone PPG, which challenges the generation of accurate and reliable BP estimates [18, 28, 87].

Second, to address low signal quality, pioneering SPW-BP studies have incorporated machine learning techniques to improve prediction accuracy [31]. While machine learning-based approaches have demonstrated superior measurement accuracy compared to traditional methods, the limited interpretability of these models poses a significant challenge to their adoption in clinical practice [56]. Transparency is critical in medical decision-making, where patients and clinicians require clear, understandable results [45, 85].

Third, while the relationship between pulse waveforms and BP has been extensively studied, most research focuses on the association between aortic BP and waveforms [60]. The pressure waveforms of the ascending aorta, however, differ significantly from those observed in the upper limbs [67] and even more so from the fingertip blood flow dynamics captured by smartphone PPG.

Fourth, existing studies on fingertip waveforms predominantly use LED-based pulse oximeters, which employ a transmission method to measure blood flow changes. This approach differs from the reflective visible light principle utilized in smartphone PPG. As a result, there is insufficient empirical evidence linking camera-based digital PPG waveform features to BP, further limiting the development of SPW-BP technologies.

Finally, a notable gap in SPW-BP research is the lack of proper benchmarking against widely accepted evaluation methods. Essential validation techniques, such as Bland–Altman analysis, and adherence to medical standards set by organizations like the British Hypertension Society (BHS), the International Organization for Standardization (ISO), the European Society of Hypertension (ESH), and the American National Standards Institute (ANSI), are often overlooked. This oversight undermines the credibility and comparability of SPW-BP findings within the field.

This study aims to bridge the gap in existing research by addressing the accuracy–interpretability dilemma in BP measurement using smartphone PPG. It focuses on

enhancing data quality, integrating interpretable machine learning, and establishing robust benchmarks for performance evaluation.

First, the study emphasizes the importance of robust data preprocessing, challenging the prevailing trend in SPW-BP research of prioritizing complex models over foundational data preparation techniques [2]. Methods such as normalization with body height, low-quality sample removal, boundary data reconstruction, and collinearity elimination are implemented to improve data integrity and the reliability of subsequent analyses.

Second, interpretable machine learning methodologies are incorporated into waveform-based BP analysis to address the limitations of black-box models, which, while often highly predictive, lack the interpretability required in medical applications [54]. By employing SHapley Additive exPlanations (SHAP), the study visualizes key features in BP prediction, improving model transparency and providing insights into critical predictors [47].

Third, this research conducts an extensive examination of fingertip waveform features collected via reflected light sources, a method distinct from the transmission-based approaches commonly used in pulse oximetry. Three feature types—including time-domain, curvature, and frequency-domain features—are systematically analyzed. Additionally, novel feature extraction techniques are introduced to account for smartphone camera functions such as autoexposure and white balancing.

Finally, the Bland–Altman method, a gold standard in medical engineering, is employed to evaluate the agreement between the proposed BP prediction technique and automated sphygmomanometer references. Results are reported following the IEEE and EHS standards, as recommended by Qin et al. [71] and Stergiou et al. [79], to ensure comparability with other medical devices.

Results

Statistical analysis

The MLR model and stepwise regression analysis revealed statistically significant multivariate relationships between waveform characteristics and BP measures. For SBP, DBP, and PP, the MLR models achieved p-values < 0.001, with adjusted r-squared values of 0.55, 0.48, and 0.38, respectively. In the bi-directional stepwise regression, the adjusted r-squared values were 0.53, 0.46, and 0.36 for SBP, DBP, and PP, respectively, indicating that stepwise regression effectively captures the multivariate relationships between waveform features and BP measures (Table 1). The AIC criterion identified gender, age, A, rPSD2, E, F/A, H, and G as key waveform features (i.e., features appearing at least twice in the table) for BP prediction.

The univariate regression analysis, using Bonferroni-corrected p-values, identified several features with statistically significant correlations to BP variables (Table 2). Among these, non-waveform features such as gender and height exhibited the strongest associations. Additionally, multiple time-domain features (e.g., NT, ESI, ERI, EPPT, AI, DT, A1, IP, RCA), frequency-domain features (e.g., rPSD4, rPSD6), and curvature waveform features (e.g., A, B) also showed strong correlations. The frequency of their occurrence in the table further underscores their relevance to BP measures.

To ensure comparability with machine learning models, cross-validation was performed for the MLR model using all features and participant-based data splitting

Table 1 Stepwise regression results

SBP (adj-R^2=0.53)		DBP (adj-R^2=0.46)		PP (adj-R^2=0.36)	
Variable	**Coefficient**	**Variable**	**Coefficient**	**Variable**	**Coefficient**
Gender	15.8027	Gender	11.5243	Gender	4.9268
Age	− 0.3664	A	0.114	HR	− 0.2763
A	0.1927	rPSD2	− 20.1424	A	0.0665
rPSD2	− 44.3025	ERI	48.7859	G	− 2.1131
IPA	16.0927	H	− 1.0149	Age	− 0.4035
E	− 0.1927	F/A	43.9614	NV	17.1607
F/A	73.6044	E	− 0.1384	SPS	− 0.8273
H	− 1.7415	DT	− 16.2778	NHA	2.0402
G	− 2.9758			FPH	26.6848
FS	21.6153				
EPPT	− 30.2194				

(Fig. 2). Under this approach, the R^2 values for SBP, DBP, and PP were 0.37, 0.30, and 0.18, respectively. The MAE values were 7.75, 6.35, and 4.49 mmHg for SBP, DBP, and PP, respectively. These findings highlight the trade-off between interpretability and predictive performance when comparing MLR to machine learning approaches.

Machine learning analysis

This study evaluated three commonly used machine learning models—SVM, RF, and MLP—and found that RF demonstrated similar overall performance to MLP and outperformed SVM. However, since RF is more interpretable due to its feature importance values, it was selected for further analysis in the remainder of the study.

With non-waveform features

The RF models were trained using an 80%-20% random train–test split for a single iteration, incorporating all available features, including four non-waveform variables such as heart rate, height, gender and age. The model based on stratified data splitting demonstrated acceptable prediction accuracy for SBP, DBP, and PP, with R^2 values of 0.43, 0.38, and 0.18, respectively. The corresponding MAE values were 7.34, 5.79, and 4.45 mmHg. The RF model based one randomly split data demonstrated superior predictive performance for SBP, DBP, and PP, achieving r-squared values of 0.74, 0.74, and 0.72, respectively (Figure 3). The corresponding MAE values for these predictions were 4.78, 3.53, and 2.24 mmHg, respectively.

SHAP analysis using participant-based data splitting produced results largely consistent with those from random data splitting. The results indicated that gender was the most influential predictor for all three dependent variables. Additionally, time-domain features such as ESI, ERI, CT, DT, and NT; frequency-domain features like rPSD6; curvature features such as A; and non-waveform variables, including heart rate and height, were consistently identified as key predictors.

Table 2 Single variate regression analysis

SBP					DBP					PP				
Variable	**n**	**B1**	**B0**	**corr**	**Variable**	**n**	**B1**	**B0**	**corr**	**Variable**	**n**	**B1**	**B0**	**corr**
Gender	630	15.95	96.06	0.64	Gender	630	10.54	59.13	0.55	Gender	630	5.41	36.93	0.45
Height	630	0.69	− 11.11	0.44	Height	630	0.46	− 12.89	0.39	DT	630	21.59	25.98	0.34
NT	627	− 147.3	152.14	− 0.29	ESI	630	0.05	34.12	0.35	rPSD6	625	2875.2	− 1955.56	0.34
ESI	630	0.04	75.78	0.26	NT	627	− 130.32	106.67	− 0.33	rPSD4	626	719.86	− 461.82	0.32
rPSD6	625	4475.16	− 3000.84	0.26	EPPT	629	− 102.01	103.03	− 0.28	HR	630	− 0.19	53.83	− 0.31
rPSD4	626	1064.72	− 637	0.23	ERI	629	50.64	53.38	0.25	Height	630	0.23	1.77	0.30
A	630	0.11	82.52	0.21	NH	630	18.5	72.95	0.22	rPSD5	625	1175.76	− 777.21	0.23
B	630	0.04	98.58	0.20	SPH	630	21.68	64.34	0.22	rPSD3	630	64.3	37.69	0.22
ERI	629	49.73	93.67	0.19	A1	628	− 105.2	87.92	− 0.22	A2	630	20.58	36.41	0.19
EPPT	629	− 88.61	138.15	− 0.19	A	630	0.08	48.37	0.2	IPA	630	4.54	36.33	0.19
AI	630	10.75	99.4	0.18	B	630	0.03	60.81	0.17	IP	630	− 3.94	41.17	− 0.18
DT	630	22.96	90.34	0.18	IHAR	629	− 4.36	67.82	− 0.16	CT	630	− 31.4	35.15	− 0.17
IPA	630	8.87	98.02	0.18	AI	630	6.62	61.61	0.15	AI	630	4.13	37.8	0.15
B/A	630	8.17	99.16	0.16	FN	629	− 44.51	78.97	− 0.15	RCA	603	− 11.29	45.45	− 0.15
A1	628	− 100.44	126.97	− 0.16										
IP	630	− 7.02	107.28	− 0.16										
RCA	603	− 23.92	116.6	− 0.16										

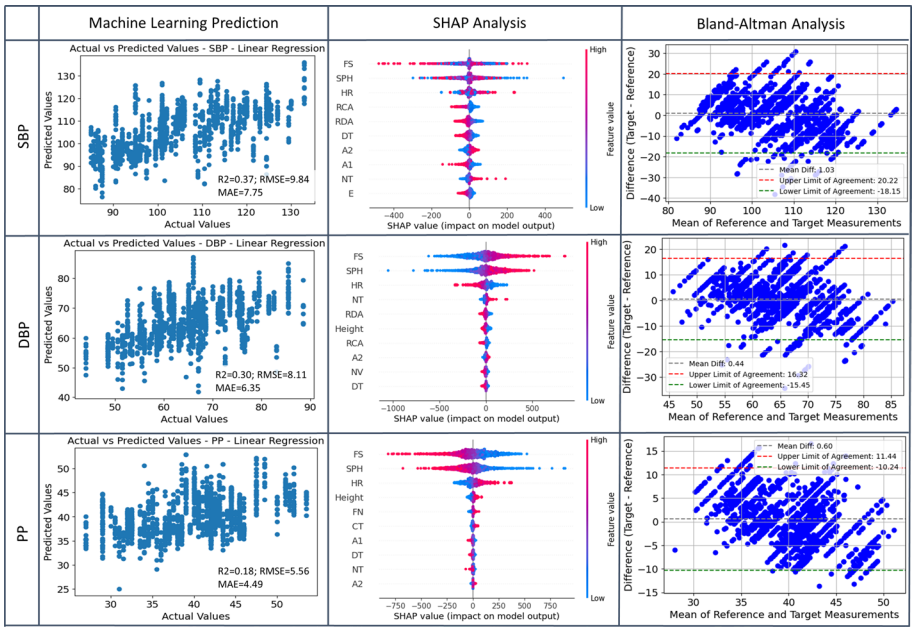

Fig. 2 Correlation analysis, SHAP analysis, and Bland–Altman analysis of the predicted blood pressure values (y-axis) versus the reference blood pressure values (x-axis) for the MLR models with data splitting by participants

Without non-waveform features

Given the significant role of non-waveform features highlighted by SHAP analysis, we conducted further evaluations by excluding these features from the RF model. As expected, the predictive performance of the RF models declined for SBP, DBP, and PP in both randomly split and stratified datasets (Figure 4). Despite this reduction in performance, SHAP analysis indicated that the key waveform features remained consistent, regardless of the inclusion of non-waveform features. Notably, IP, B, and B/A emerged as important features only when gender, height, and HR were excluded from the analysis.

Outlier and collinearity removal

Removing outliers is a common practice in data analysis, as it can improve model performance by eliminating extreme values that may distort results. High correlations among predictors, however, can lead to counterintuitive, unstable, and misleading outcomes in statistical analyses [10]. In this study, we examined the impact of these two data preparation techniques using only SBP data. First, we removed 45 data points in which at least five independent variables fell outside three times the interquartile range (below the first quartile or above the third quartile). For the RF model incorporating all waveform features with random data splitting, outlier removal did not significantly improve r-squared values or substantially reduce MAE. Additionally, the key features identified by the SHAP analysis remained largely unchanged (Figure 5).

This study then evaluated the necessity of collinearity removal using the approach outlined by Dormann et al. [17], where variables with lower correlations to the target were removed from pairs exhibiting correlation coefficients above specific thresholds

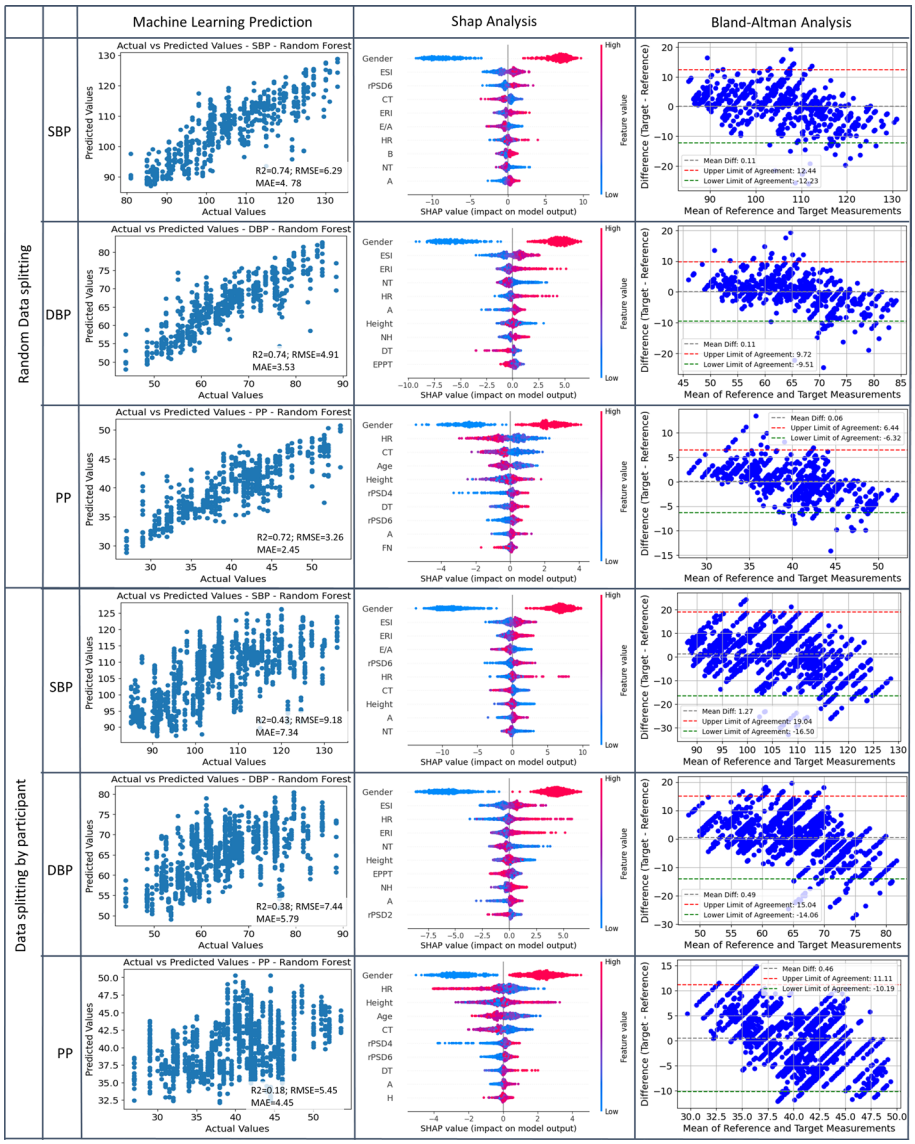

Fig. 3 Correlation analysis, SHAP analysis, and Bland–Altman analysis were performed to assess the relationship between predicted blood pressure values (y-axis) and reference blood pressure values (x-axis) from the RF models, incorporating both waveform and non-waveform features

(Table 3). The results showed that collinearity removal marginally improved the RF model's accuracy, although these improvements were not statistically significant. Nonetheless, the process led to minor shifts in the identified important features. For example, at a threshold of r = 0.95, newly identified important waveform features included EPPT, ERI, CT, E/A, and rPSD4.

The baseline analysis

The baseline model, which included only non-waveform features, was trained using an 80%-20% data split, both randomly and stratified by participants. The prediction accuracies with stratified data for SBP, DBP, and PP had r-squared values of 0.24, 0.11,

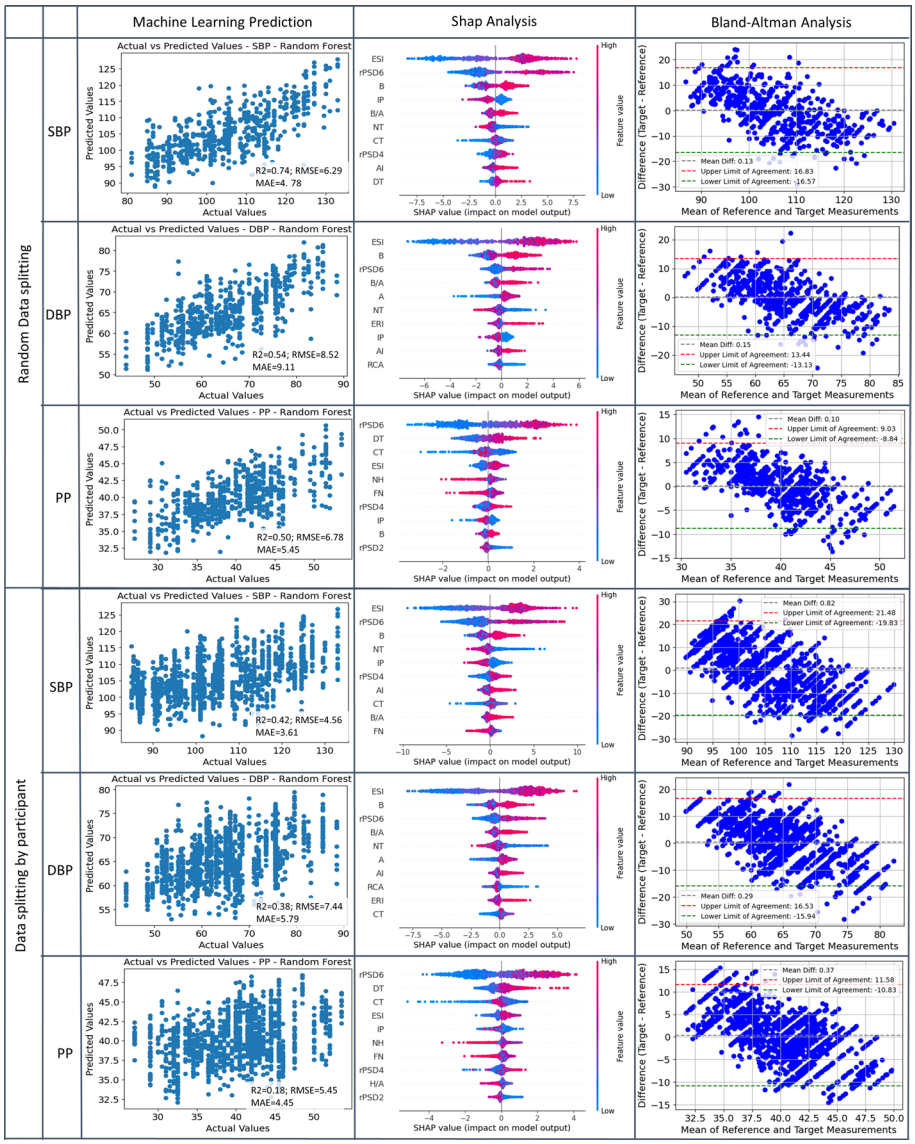

Fig. 4 Correlation analysis, SHAP analysis, and Bland–Altman analysis were conducted to assess the relationship between predicted blood pressure values (y-axis) and reference blood pressure values (x-axis) from the RF models utilizing only waveform features

and 0.12, respectively (Fig. 6). The corresponding MAE values were 9.14, 7.78, and 5.04 mmHg. Comparing these values with the results from the analysis including non-waveform features presented above, we see that incorporating waveform features increases the r-squared values to 0.43, 0.38, and 0.18, respectively. These results validate the importance of waveform features in prediction.

We also compared the results using random sampling. The prediction accuracies with randomly split data for SBP, DBP, and PP had r-squared values of 0.96, 0.97, and 0.98, respectively. The corresponding MAE values were 0.57, 0.44, and 0.26 mmHg. These results highlight the issue of data leakage.

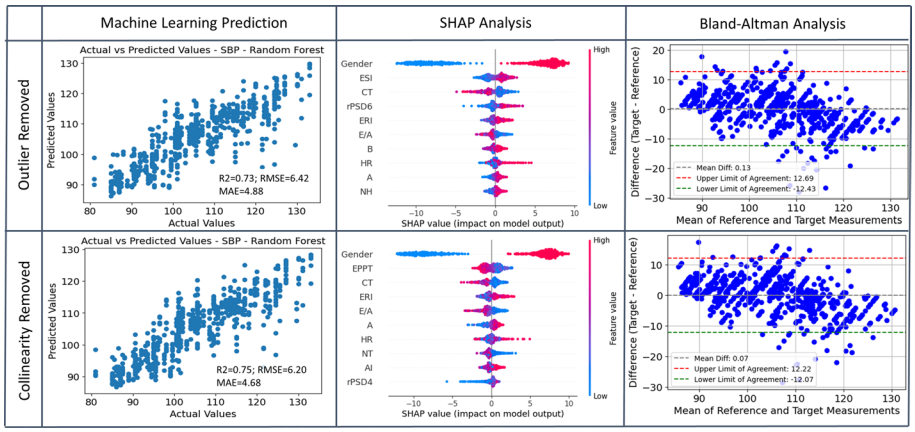

Fig. 5 Correlation analysis, SHAP analysis, and Bland–Altman analysis were conducted to assess the relationship between predicted SBP values (y-axis) and reference SBP values (x-axis) from the RF models after outlier removal and collinearity correction

Table 3 Collinearity removal comparison

Collinearity threshold (*R*)	No. of variables removed	RF accuracy (R^2)
0.7	29	0.67
0.75	24	0.76
0.8	20	0.76
0.85	18	0.76
0.9	10	0.75
0.95	8	0.75
No	0	0.74

Reference comparisons and Bland–Altman analysis

When the data were stratified by participants, the mean and standard deviation of prediction errors for SBP, DBP, and PP increased to 1.27 ± 9.07 mmHg, 0.49 ± 7.43 mmHg, and 0.46 ± 5.44 mmHg, respectively. According to Stergiou et al. [78], these results for SBP and DBP were not acceptable, as the percentages of errors ≤10 mmHg were 73.49% and 82.14%, both falling below the 85% threshold (Table 4). Additionally, Stergiou et al. [79] recommend that cuffless devices achieve an MAE of less than 6% compared to the reference device. Therefore, the proposed method was not acceptable for SBP and DBP when data were stratified by participant ID, except when non-waveform features were included.

Bland–Altman analysis revealed that approximately 95% of the differences between the predicted and reference values fell within the upper and lower limits, indicating a high level of agreement with the reference. However, the Bland–Altman plot also identified a systematic bias in the predictions.

On the other hand, when all features were included and data were split randomly, the mean prediction errors for SBP, DBP, and PP were 0.11 ± 6.30 mmHg, 0.11 ± 4.91 mmHg, and 0.06 ± 3.26 mmHg, respectively. According to Stergiou et al. [78], the proposed method is acceptable for SBP and DBP estimation, as the percentages of

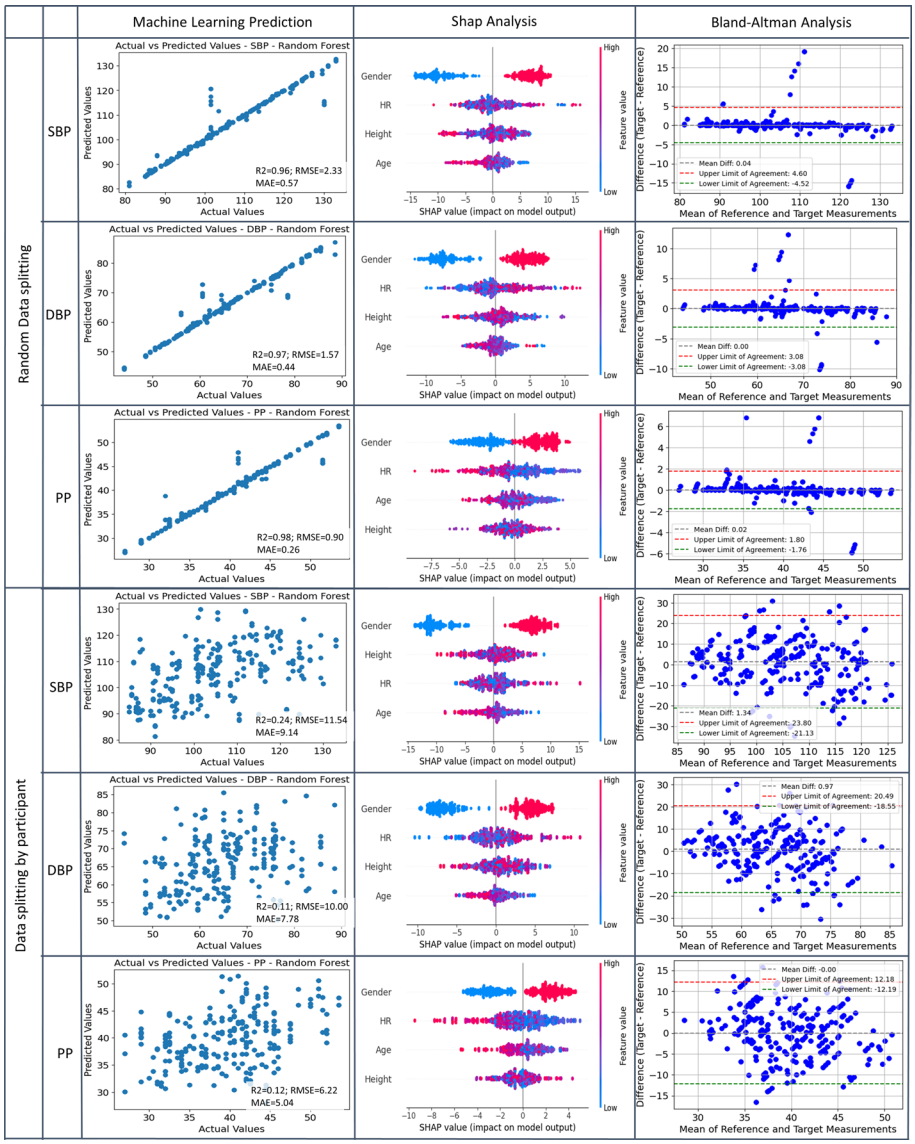

Fig. 6 Correlation analysis, SHAP analysis, and Bland–Altman analysis were conducted to assess the relationship between predicted blood pressure values (y-axis) and reference blood pressure values (x-axis) from the baseline RF models

errors ≤10 mmHg were 89.84% and 94.29%, both exceeding the 85% threshold. Based on the BHS grading system, the SPW-BP method achieved Grade A.

When only waveform features were included, the mean and standard deviation of prediction errors for SBP, DBP, and PP were 0.13 ± 8.53 mmHg, 0.15 ± 6.78 mmHg, and 0.10 ± 4.56 mmHg, respectively, for random data splitting, and 0.82 ± 10.54 mmHg, 0.29 ± 8.29 mmHg, and 0.37 ± 5.72 mmHg, respectively, for data splitting by participants. The percentage of errors within 10 mmHg indicated that, when only waveform features were included, the proposed method did not meet the acceptance criteria based on reference agreement analysis.

Table 4 Bland–Altman analysis

	Random data split			Stratified by participants		
	SBP	DBP	PP	SBP	DBP	PP
All features						
Within limit %	94.76	94.13	94.76	95.91	94.57	95.75
Error mean (mmHg)	0.11	0.11	0.06	1.27	0.49	0.46
Error SD (mmHg)	6.30	4.91	3.26	9.07	7.43	5.44
R^2	0.74	0.74	0.72	0.44	0.38	0.18
RMSE	6.29	4.91	3.26	9.15	7.44	5.45
MAE (mmHg)	4.78	3.53	2.45	7.34	5.79	4.45
SD of MAE	0.36	0.29	0.25	0.87	0.72	0.54
Error < 5 mmHg (%)	62.86	75.40	88.73	39.34	52.95	59.24
Error < 10 mmHg (%)	89.84	94.29	99.21	73.49	82.14	93.62
Error < 15 mmHg (%)	97.62	98.89	100	90.40	95.28	100
Waveform features only						
Within limit %	95.08	95.87	93.97	96.62	96.62	95.04
Error mean (mmHg)	0.13	0.15	0.10	0.82	0.29	0.37
Error SD (mmHg)	8.53	6.78	4.56	10.54	8.29	5.72
R^2	0.54	0.50	0.42	0.23	0.23	0.10
RMSE	8.52	6.78	4.56	10.57	8.29	5.72
MAE (mmHg)	6.91	5.45	3.62	8.70	6.83	4.60
SD of MAE	0.32	0.41	0.28	0.47	0.53	0.78
Error < 5 mmHg (%)	41.90	53.01	73.97	31.94	40.91	61.52
Error < 10 mmHg (%)	75.40	84.28	96.35	62.79	75.06	91.90
Error < 15 mmHg (%)	93.02	97.94	100	82.53	94.02	99.92

Discussion

Principal findings

The feasibility of using waveform features in BP estimation

Our data support the proposed strategy, demonstrating that enhanced data preprocessing can significantly improve prediction accuracy. This benefit extends to both more interpretable traditional statistical methods and less interpretable machine learning models. The MLR analysis, which offers greater transparency, yielded statistically significant results for SBP, DBP, and PP, with adjusted r-squared values of 0.37, 0.30, and 0.18, respectively, and p-values less than 0.001. In contrast, the RF model, under the same data-splitting condition, achieved higher prediction accuracy with r-squared values of 0.43, 0.38, and 0.18 for SBP, DBP, and PP, respectively. These results highlight that while MLR provides an interpretable approach, the RF model slightly enhances prediction accuracy.

Additionally, since the r-squared values for the baseline model were only 0.24, 0.11, and 0.12, this improvement underscores the significant contribution of waveform features in enhancing BP prediction accuracy.

When compared to previous studies, our models, incorporating all features, demonstrate competitive performance in terms of MAE. Gao et al. [27], using discrete wavelet transform for feature extraction from oximeter PPG signals and a nonlinear SVM for prediction, reported MAEs of 5.1 mmHg for DBP and 4.6 mmHg for SBP. Similarly, Dey

et al. [15] analyzed 233 time–frequency domain features with an infrared heart rate sensor on a Samsung Galaxy S6, employing Lasso regression, and achieved MAEs of 5.0 mmHg for DBP and 6.9 mmHg for SBP. In comparison, our RF model, with data stratified by participants, produced MAEs of 7.34 mmHg for SBP and 5.79 mmHg for DBP. These findings, consistent with those of Steinman et al. [77], confirm that our approach aligns well with existing methods in terms of prediction accuracy.

For the data-splitting methods, models with random data splitting consistently outperformed those with participant-stratified data splitting. While data stratification resulted in a slight reduction in performance, this more conservative splitting method is preferable for ensuring the generalizability and reliability of the model.

Feature importances

There is no consensus on which waveform features are most significantly related to BP measurements. Some studies suggest that waveform characteristics are predominantly associated with DBP [8], while others argue for a stronger correlation with SBP [9]. Additionally, several studies have proposed a relationship between waveform features and both SBP and DBP [38]. In this study, our correlation analysis revealed significant associations between waveform features and all BP measures.

Time-domain indices have previously been linked to both SBP and DBP. For instance, arterial aging is typically positively correlated with RI and negatively correlated with PPT [53]. Other studies have demonstrated a significant positive correlation between SI and pulse wave velocity [64]. In contrast, features such as CT and DT have been shown to be negatively correlated with BP measurements [84]. Our findings align with these prior studies, showing strong correlations between time-domain indices and both SBP and DBP. In particular, the proposed remedy for dampened waveforms yielded promising results. ESI and ERI exhibited strong positive correlations with both SBP and DBP in both MLR and RF models, while EPPT showed a strong negative correlation. This suggests that adjusting for issues created by the autoexposure function of smartphone cameras significantly enhances BP predictability.

Research also indicates that acceleration PPG indices are associated with arterial stiffness, age, the risk of heart attack, and peripheral artery distensibility [19]. Compared to individuals with normal BP, those with hypertension tend to show lower B/A and C/A ratios but higher D/A and E/A ratios [76]. In our data, the A, B, and B/A indices consistently showed strong positive correlations with SBP and DBP, while other variables exhibited less pronounced associations with BP measurements.

While previous cardiovascular studies have explored the frequency-domain features of waveforms [13], this study, to our knowledge, is the first to link these features directly to BP. Our results indicate that the power spectral densities at frequencies PSD4 and PSD6 are positively associated with BP.

We also explored the impact of incorporating non-waveform features, such as gender, heart rate, and body height, on prediction accuracy. As anticipated, including these non-waveform features significantly improved model performance. This approach draws on prior studies that often add non-waveform features to machine learning models, resulting in high accuracy in pulse waveform-based BP prediction [25]. However, this high accuracy may be partly due to the inclusion of non-waveform variables, highlighting

the importance of ensuring interpretability in machine learning to avoid misleading conclusions.

The optimal feature selection method remains a subject of debate. In multivariate analyses, stepwise regression and MLR often identify different feature sets. While some researchers favor AIC [30], others argue for using p-values, confidence intervals, or information-theoretic criteria to summarize statistical information [57]. In our study, univariate and multivariate analyses yielded different sets of significant features, with some features that were crucial for BP prediction showing low importance in SHAP analysis. This highlights the complexity of feature selection in both machine learning and statistical modeling. While the primary aim of this study was not to identify the best feature set, these findings open avenues for future research to explore optimal feature selection strategies.

Limitations and suggestions

Low signal quality

Our study underscores the potential of smartphones for BP prediction, although the method did not meet established accuracy criteria. The limited accuracy may be attributed to factors such as low signal quality and the inherent variability of PPG signals, which are influenced by skin tone, age, gender, and environmental conditions [23]. Additionally, external factors like ambient light and motion artifacts caused by unstable phone handling further complicate the consistency of the signals.

Another potential contributor to BP estimation errors is the low data sampling rate. However, there is no consensus on the minimum sampling rate required for accurate BP estimation using PPG. Laborde et al. [80] recommend a minimum of 125 Hz for HRV studies, while Béres and Hejjel [5] suggest a minimum of 5 Hz for average heart rate estimation in healthy subjects without interpolation. Despite the lack of consensus, smartphones typically capture data at a frame rate of 30 frames per second [44]. Our findings suggest that this frame rate may be sufficient for BP estimation, highlighting the potential of smartphones to provide reliable BP measurements despite lower sampling rates.

To enhance signal acquisition quality, several techniques have been proposed, including the identification of optimal color channels and regions of interest (ROI) [58], noise detection in samples [4], and filtering of high-quality samples based on signal quality standards [44]. Additionally, smartphones with higher sampling rates may improve overall signal quality. In terms of data analysis and processing, recent advancements in LED-based PPG research have introduced deep learning models, such as CNN and LSTM [83], which have successfully reduced MAE to 4.06 mmHg for SBP and 3.33 mmHg for DBP [22].

Data splitting method

Collecting multiple data points from a single participant is common in bioengineering studies [32, 83]. However, machine learning models often use random data splitting without considering participant grouping, which can lead to overfitting. This may explain the high prediction accuracy reported in some SPW-BP studies. In our study, participant-based splitting significantly reduced model accuracy. For instance, the MAE for SBP prediction increased from 4.78 mmHg with random splitting to 7.34 mmHg

with participant-based splitting. This suggests that models may rely on individual characteristics rather than true waveform–BP relationships. These findings emphasize the need for thoughtful data-splitting strategies to ensure robust, generalizable results.

Collinearity and outlier removal

Collinearity presents a significant challenge in data analysis, with various strategies available to address it [10]. Common techniques, such as principal component analysis (PCA) and ridge regression, are often employed; however, these methods can reduce the interpretability of results. Alternatively, selecting representative variables can help mitigate collinearity but may introduce bias and compromise model accuracy [17]. In this study, we applied a straightforward variable removal approach to enhance model interpretability while minimizing bias. This method effectively reduced collinearity, but it led to a decrease in the adjusted r-squared values of our models. This outcome underscores the inherent trade-off between model interpretability and accuracy, highlighting the complexity of addressing collinearity in data analysis.

Limited participant diversification

Assessing BP through waveforms is fundamentally based on the relationship between vascular sclerosis and the speed of reflected waves, which directly influences BP measurements. However, factors beyond vascular sclerosis also significantly impact BP. For instance, aging induces physiological changes, such as increased collagen deposition and skin thinning, which alter PPG signals by affecting both BP and light transmission through the skin. Moreover, PPG signals are highly dependent on peripheral circulation, with poor circulation leading to degraded signal quality. Consequently, SPW-BP may lack robustness across different age groups, underscoring the need for further investigation to assess the generalizability of these findings.

Issues with referencing methods

For BP reference, the auscultation method and intra-arterial measurements are considered the gold standards. The IEEE 1708-2014 standard [33] also recommends using a mercury sphygmomanometer for comparison. However, for practical reasons and to reduce experimental costs, this study used an automated sphygmomanometer as the reference device. While automated sphygmomanometers provide convenience, they may introduce additional estimation errors compared to gold standard methods.

In addition, the IEEE 1708-2014 standard [33] includes a calibration process, and Stergiou et al. [79] emphasized pulse waveform-based BP estimation as a technology requiring user cuff calibration. However, since this study served as a proof of concept rather than introducing a new BP measurement device, we did not calibrate the device. Instead, we collected average BP readings before and after the measurement process, using part of the data to train the RF model and the rest for validation. Therefore, the trained model in our study should not be used directly as a BP measurement device, as it still requires calibration if future studies aim to adapt it for real-world applications.

PPG color channel choice

The choice of color channels for PPG technology has been extensively discussed in the literature. Blood perfusion variations depend on the wavelength of light, as different wavelengths penetrate and reach the vascular bed at varying depths within the skin. Red light (620 nm) penetrates deeper, reaching several centimeters into blood vessels, while blue light (432 nm) penetrates less than 1 mm. As a result, the red channel has been frequently used in previous studies [46].

In contrast, Maeda et al. [48] compared green and infrared light, finding that green light offered greater robustness. Similarly, Lee et al. [42], in a study comparing green, red, and blue light, identified green light as the most effective for reflected light estimation. In smartphone PPG studies, Gao et al. [27] also recommended green as the optimal color band over blue and red. Additionally, some studies have utilized all three color bands to estimate pulse waveforms [14].

Based on our experience, single-channel signals—regardless of the channel's performance—are particularly susceptible to motion artifacts when recording skin color using smartphone cameras. We found that using the weighted average of all three color channels significantly improved signal quality. Moreover, smartphone cameras often adjust color and exposure automatically, which can cause values in a single channel to reach boundary limits (0 or 255) for several frames. This limitation led us to adopt the weighted average of the three color channels, which proved to be more robust, particularly when the camera operates with an auto-exposure function. However, this approach has not been formally tested, and further analysis is necessary to confirm its effectiveness.

The true 2nd peak

PPT, RI, and SI have been identified as important peripheral BP waveform features for determining BP in both previous and current study. However, it is crucial to highlight that there is no consensus in the literature regarding the definition of the position of the second peak, which forms part of the definitions of PPT, RI, and SI. This discrepancy in definitions could undermine the consistency and validity of waveform-based cardiovascular analysis across studies.

In aortic pressure wave studies, RI is commonly defined as the ratio between the height of the reflected wave and the original wave [90]. The waveform typically consists of three distinct peaks: the early systolic peak, the late systolic peak, and the diastolic peak [40]. The first arrival of the reflected wave results in the late systolic peak, while the diastolic peak is caused by a second reflected wave [3].

However, variations exist in the identification of the second peak for peripheral pulse waveforms. Some studies use the late systolic peak as the second peak [50, 65] and define RI as the ratio of this peak to the early systolic peak. Others consider the diastolic peak as the second peak [16]. Additionally, several studies define the radial augmentation index as the ratio of the late systolic peak to the early systolic peak, while the RI is defined as the ratio of the diastolic peak to the early systolic peak [68]. A further approach does not rely on physiological knowledge of the waveform, instead identifying the second peak as the most prominent peak following the initial peak [52].

Beyond conceptual inconsistencies, there is no consensus on the technical method for identifying the second peak's location. Chowienczyk et al. [12] determined this position using the first derivative, while Elgendi [19] applied the second derivative, and Melenovsky et al. [50] proposed using the peaks of the fourth derivative. Alty et al. [1] suggested an alternative approach, utilizing an inflection point when a clear second peak is absent.

In the current study, the limited frame rate of the smartphone camera and suboptimal signal quality posed challenges in reliably identifying all three peaks in the waveform. Consequently, we followed prior studies and defined the second peak as the most prominent waveform feature visible after the initial peak [52]. While definitions may vary, both the late systolic peak and the diastolic peak are induced by reflected waves, and the arrival time of these reflected waves is influenced by vascular stiffness. Given that arteriosclerosis is strongly correlated with BP, it is reasonable to use either the diastolic or late systolic peak for BP estimation. Nevertheless, despite general similarities in the direction of waveform features, considerable differences in their magnitudes may exist. Future studies should exercise caution when making direct comparisons of these features across different definitions.

Conclusion

Smartphone-based BP measurement, valued for its convenience and cost-effectiveness, holds significant promise for enabling non-invasive, continuous BP monitoring. However, realizing this potential requires overcoming the challenge of balancing predictive accuracy with interpretability. Achieving this balance necessitates improving prediction accuracy while ensuring that the results remain clear and understandable.

The findings of this study provide empirical evidence supporting the validity of the SPW-BP method, demonstrating the use of statistical and explainable machine learning models to establish interpretable relationships between waveform features and BP measures. However, the reference agreement analysis revealed that the proposed method is currently inadequate as a substitute for traditional sphygmomanometer-based BP assessments. Further research is required to enhance the practicality and utility of the proposed method for real-world applications.

Methods

Data collection

Data were collected from 127 participants, including university students and employees in Shenzhen, China. The sample comprised 56.69% males, with an average age of 22.78 years (SD = 1.97). No specific inclusion or exclusion criteria were applied. Participants were instructed to hold a smartphone (Mi-8 SE, Xiaomi, China) in their left hand, press their finger against the camera, and use the Heartily Happy (HH) app, developed by the research team and publicly available on the Google Play Store, to record six 4-min videos of their fingertips at a resolution of 120 × 160 pixels.

Before and after the data collection session, participants measured their systolic blood pressure (SBP), diastolic blood pressure (DBP), and pulse pressure (PP, calculated as the difference between SBP and DBP) using a cuff-based automatic sphygmomanometer (HEM-6322T, Omron, Japan). The average of the pre- and post-session measurements was used as the reference for comparison. Ethical approval for

the study was granted by the Department of Psychology at Tsinghua University, and informed consent was obtained from all participants.

The study generated 766 waveform samples, with an average of 6.03 samples per participant, and 229,165 beat-to-beat intervals (BBIs), approximately 299.17 per sample. Of these, 657 samples (86%) met the validity criteria: a Smartphone PPG Signal Quality Index (PPG-SQI) above 0.6 [44] and a minimum of 30 successful heartbeats per sample.

To account for the established relationship between waveform features and heart rate (HR), time-domain features were normalized to a standard HR of 75 beats per minute, following procedures established in previous studies [38]. Considering the relationship between waveform features, height, and gender, the analysis included only height, as advised by O'Rourke et al. [63]. Time-domain features were then standardized to a height of 170 cm, except for the systolic index (SI), which does not require height normalization.

Signal processing

Convert RGB signals to waveform

In each data collection session, the HH app activates the device's built-in flashlight to record videos at a resolution of 120×160 pixels, capturing 30 frames per second, as Liu et al. [44] detailed (Fig. 7). Raw picture frames, in YUV format, are converted into RGB format. The input signals (r_i, b_i, g_i) from the red, blue, and green color channels undergo normalization, using a 100-point moving average $(\overline{R}, \overline{B}, \overline{G})$ and standard deviation $(\sigma_R, \sigma_B, \sigma_G)$ for processing. This study then calculates the standard deviation-weighted average $f(t_i)$ as follows:

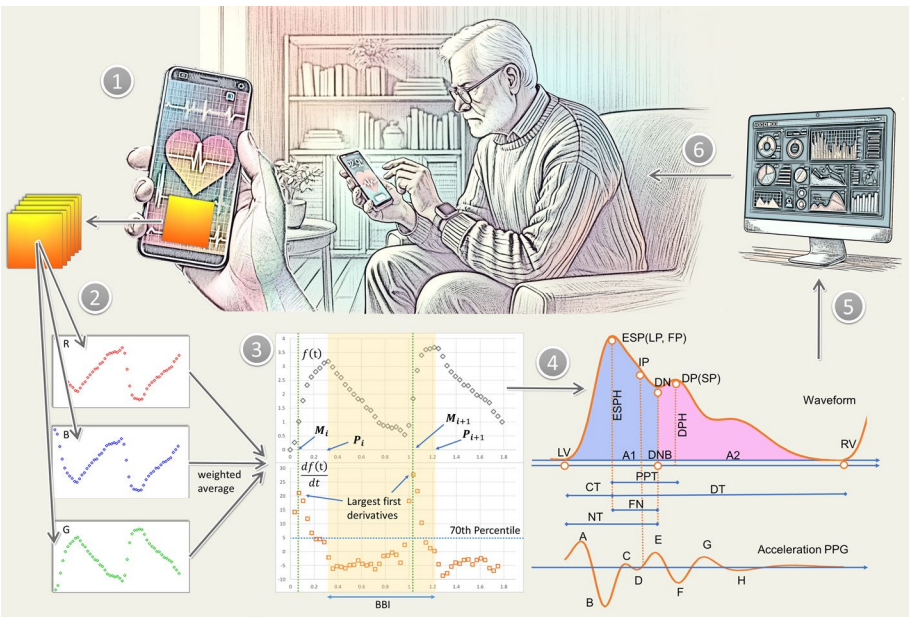

Fig. 7 The data processing flow entails: (1) collecting data; (2) converting RGB signals to waveforms; (3) determining BBIs; (4) extracting waveform features; (5) using waveform features to predict BP; and (6) providing BP estimates to users [adapted from Liu et al., [44] and Elgendi et al., [20]]

$$f(t_i) = \frac{\sigma'_G \times n_G(g_i) - \sigma'_B \times n_B(b_i) - \sigma'_R \times n_R(r_i)}{\sigma'_R + \sigma'_G + \sigma'_B}, \quad (1)$$

where,

$$\sigma_{C'} = \begin{cases} \sigma_C & \text{if } \sigma_C > 0.5, 3 < \overline{C} < 252 \\ 0 & \text{otherwise} \end{cases}, C \in \{R, B, G\}$$

and $t_i \in \boldsymbol{T} = \{t_i | i \in 1, .., k\}$ denotes the time at which the ith data point was collected. A color channel is excluded from the $f(t_i)$ if the average of the input ($\overline{C}$) either approaches the lower limit of 0 or the upper limit of 255, or if its standard deviation (σ_C) is too small ($\sigma_C \leq 0.5$). Moreover, the signs of the red and blue channels are inverted to reflect their inverse relationship with the green channel.

Beat-to-beat (BBI) segmentation

After converting signals into waveform inputs, $f(t_i)$ is segmented into intervals corresponding to each BBI, as detailed in Liu et al., [44]. The study then identifies BBIs by using a set of local maxima ($\boldsymbol{M_i}$)—those surpassing the 70th percentile (P_{70}) of the first derivatives $f\prime(t_i)$. The distances between two successive data points in the set $\boldsymbol{M}$ are converted into HRs to exclude points exhibiting an HR exceeding 150 beats per minute (bpm). The intervals segmented by the data points in $\boldsymbol{M}$ are then defined as the set of BBIs ($\boldsymbol{B}$):

$$\boldsymbol{B} = \left\{ (t_1, t_2) | t_1 \in \boldsymbol{M}, t_2 = \min \left\{ t_i \in \boldsymbol{M} | t_i > t_1, \frac{60}{t_i - t_1} < 150 \right\} \right\}. \quad (2)$$

Data points within each BBI is normalized are then normalized to mitigate issues associated with baseline drift [69]:

$$f_{\text{normalized}}(t_i) = f(t_i) + \left(\frac{t_i - t_L}{t_R - t_L} \right) \times \left(f(t_R) - f(t_L) \right), \forall t_i \in (t_L, t_R), (t_L, t_R) \in \boldsymbol{B}. \quad (3)$$

This study then applied the R package RHRV [49] to convert the heartbeat points HRV measures for further analysis.

Waveform features

This study utilizes three groups of waveform features commonly referenced in the literature (Table 5). Time-domain indicators encompass features related to the time between feature points, height differences among these points, and the waveform's area under the curve. The PPG waveform's second derivative, known as acceleration PPG, characterizes the waveform's contour curvature [82]. The frequency-domain features are the power spectral densities (PSD) generated by the fast Fourier transform (FFT) and several derived values from the PSDs (Figure 8). Although studies typically use the heights of the peaks to represent the relative strengths of harmonics, due to the susceptibility of spike heights to random noise, this study uses the curve's area under the curve (approximating the interval's average value) for a more accurate representation of relative strength. For each sample, we use the median of the values obtained from all the BBIs to represent the sample.

Table 5 Waveform features

SN	Name	Definition and calculation details
Time-domain features (Fig. 7—part 4)		
1	Crest time (CT)	The interval between the left valley (LV) and ESP [41]
2	Diastolic time (DT)	The interval between ESP to the right valley (RV) [84]
3	FN	ESP to DN
4	FirstPeakHeight	The height of first peak
5	HeightDifferenceFirstPeak ToSecondPeak (FS)	ESP to DN
6.~8	Inflection point area (IPA) A1 A2	The diastole to systole area ratio is calculated from the area under the curve from IP to RV (A2) relative to the area from LV to IP (A1) (L. [88]). The inflection point (IP), defined as the last point before DP where the first derivative shifts from positive to negative, is crucial in calculating the IPA. Points E or DN demarcate the diastolic and systolic areas [11, 75], with A1 approximated as a polygon formed by LV, ESP, DN, and DNB, and A2 as a triangle comprising IP, DN, and RV, simplifying the calculation process
9	IP	The ratio of second peak is not obvious so the inflection point is used as the second peak
10	IP slope	The slope of the wave at inflection point
11	Peak-to-peak time (PPT)	The interval between the early systolic peak [ESP, also known as the left peak (LP) or the first peak (FP)] and the diastolic peak (DP). The right valley (RV) is the lowest point in the BBI, and the preceding BBI's RV is termed the left valley (LV). The diastolic peak [DP, or second peak (SP)], is the first point between ESP and RV with a zero first derivative and a negative second derivative. If no second peak exists between ESP and RV, indicating a consistently negative slope from LP to RV, the DP is identified as the point with the minimum second derivative between ESP and RV
12	Notch height (NH)	The lowest point between ESP and DP is the dicrotic notch (DN)
13	Notch time (NT)	The interval between LV to the dicrotic notch (DN). In cases without a second peak, IP is designated as DN
14	Notch to valley time (NVT)	The interval between DN to right valley (RV)
15	RCA	The ratio of CT to NT
16	RDA	The ratio of NT to the combined duration of CT and DT
17	Reflection index (RI)	The ratio of the diastolic peak height (DPH) to the early systolic peak height (ESPH)
18	Stiffness index (SI)	The ratio of body height to PPT [6] [18]
19	SR	DP to RV
20	SPH	The second peak height
21	SecondPeakSlope	The slope at second peak

Table 5 (continued)

SN	Name	Definition and calculation details
Curvature features (acceleration PPG, Fig. 7*—part 4)*		
22	A	The first local maximum of the second derivative, determined by the point with the largest second derivative before ESP
23	B	The first local minimum of the second derivative, determined by the point with the smallest second derivative before ESP
	C	The second local maximum of the second derivative, determined by the point with the largest second derivative point B and point E. (Not included in the data analysis.)
	D	The second local minimum of the second derivative, determined by the point with the smallest second derivative between point B and point E. (Not included in the data analysis.)
24	E	The third local maximum of the second derivative, determined by the point with the largest second derivative between ESP and point F
25	F	The third local minimum of the second derivative, determined by the point with the smallest second derivative between the ESP and RV
26	G	The fourth local maximum of the second derivative, determined by the point with the largest second derivative between point F and point H
27	H	The fourth local minimum of the second derivative, determined by the point the smallest second derivative between point F and RV
28.~32	BA, EA, FA, GA, HA	|B/A|, |E/A|, |F/A|, |G/A| and |H/A|. Given that B/A, E/A, F/A, G/A and H/A are negative, we converted them to their absolute values for a more intuitive interpretation
33	Aging index (AI)	BA– EA. AI is usually defined as BA—(CA + DA + EA) [7]. However, in this study, AI is defined as the difference between BA and EA only, due to difficulties in identifying points C and D with poor signal quality and the fact that the values of C and D are close to zero
*Frequency-domain features (*Fig. 8*)*		
34.~39	PSDi	The *i*th relative power spectrum density. The continuous PSD curve is segmented using the midpoints between each peak. We define the strength of the *i*th harmonic (PSD_i, starting from 1) as the area between the *i*th midpoint and the (i + 1) th midpoint. Since the absolute values of each raw PSD_i is influenced by the quality of the signal, the values are normalized as the relative values: $PSDi = \frac{rawPSD_i}{\sum_{j=1}^{6} rawPSD_j}$
40	NHA	$1 - PSD1$[8]
41	IHAR	1-NHA/IPA [8]

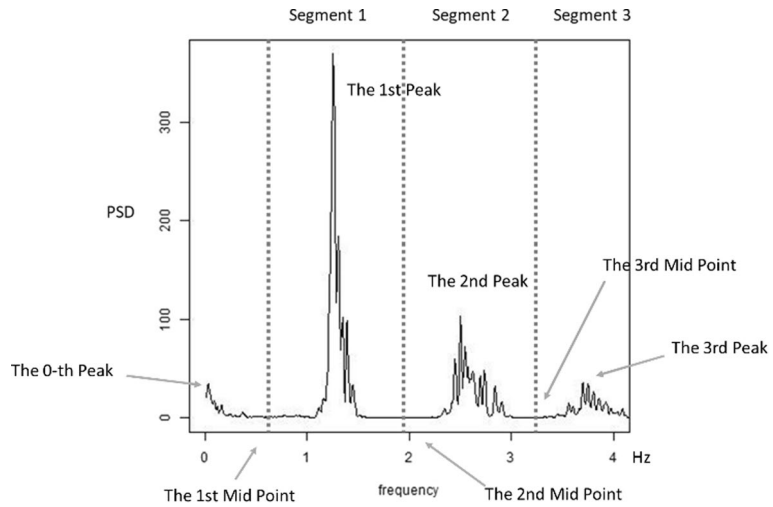

Fig. 8 An illustration of the PSD generated by FFT and the segmentation

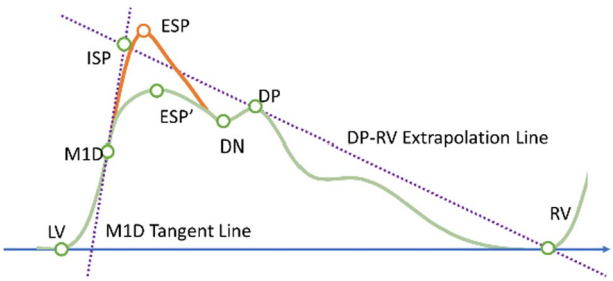

Fig. 9 Comparison between the theoretical pulse waveform [26] and observed results obtained using the Heartily Happy (HH) app

Initial analysis revealed that our waveforms were smoother than the theoretical model depicted by the green line in Fig. 9, with a reflection index (RI) lower than values previously reported, around 0.85 [65]. We attribute this discrepancy to the auto-exposure adjustment feature of smartphone cameras. To optimize image quality for human vision, the operating system modifies pixel RGB values to maintain a visually comfortable average. However, since RGB values are limited to a 0 to 256 range, this adjustment may compress boundary values. Consequently, this compression results in a dampened waveform, evident from the average pixel values, particularly when pixels approach the RGB scale's extremities [39].

To address this issue, we introduce a new method for estimating the ESP height. Our method calculates the ESP height using the intersection point (ISP, Fig. 9) of the tangent line at the point of maximum first derivative and the extrapolation line connecting DP and RV. Subsequently, we define the Expected Reflection Index (ERI) as the ratio of the DP height to the ISP height. Furthermore, we introduce the Adaptive Reflection Index (ARI), set equal to ERI when the BA is less than or equal to 1, and equal to the RI when BA exceeds 1. Since the definition of SI and PPT are also influenced by the position of ISP, we define EPPT as the time from IPS to DP and ESI as the ratio of body height to EPPT.

Statistical analysis

This study first utilizes the multiple linear regression (MLR) model to demonstrate the feasibility of predicting BP using statistical analysis alone. Next, stepwise regression is applied, which iteratively adds or removes variables to optimize the Akaike Information Criterion (AIC) value [86]. Finally, single-variable linear regression models are employed to examine the correlation between individual waveform features and BP measures.

Given the inclusion of 45 independent variables and 3 dependent variables in the analysis (8 frequency-domain features, 12 curvature-domain features and 21 time-domain features and 4 non-waveform features), the Bonferroni correction was applied to mitigate selection bias. The significance threshold for p-values was set at$3.7 \times 10^{-4}[= 0.05/(3 \times 45)]$, ensuring robust statistical validity.

Machine learning model

This study evaluated three commonly used machine learning models: support vector machine (SVM), random forest (RF), and multilayer perceptron (MLP). We also compared RF models that use user-stratified samples with those that use random data splitting. Since each participant provided multiple sample, data splitting randomly might produce data leakage. However, many existing machine learning research did not consider this fact or did not explicitly explain the data splitting strategy in their research.

Reference comparison and Bland–Altman analysis

To validate the accuracy of the proposed method, this study compares its results with those obtained using a reference automated sphygmomanometer and evaluates the findings based on standards established by the BHS, ISO, ESH, and ANSI.

Recognizing the variation in accuracy requirements among these organizations, Stergiou et al. [78] recommend adopting a consensus of the standards, which consider a device acceptable if the probability of a tolerable error ($\leq$10 mmHg) is at least 85%. The BHS standard further grades BP measurement devices based on cumulative frequency error percentages: Grade A (60% < 5 mmHg; 85% < 10 mmHg; 95% < 15 mmHg), Grade B (50% < 5 mmHg; 75% < 10 mmHg; 90% < 15 mmHg), and Grade C (40% < 5 mmHg; 65% < 10 mmHg; 85% < 15 mmHg) [62]. The consensus proposed by Stergiou et al. [78] aligns with the Grade A requirements of the BHS standard, providing a rigorous benchmark for evaluation.

For cuffless devices, Stergiou et al. [79] summarized the requirements outlined in IEEE 1708-2014, IEEE 1708a-2019 standards [33, 34], and ISO 81060-3 standard [35]. They concluded that a device should achieve a MAE of less than 6% compared to the reference device. In this study, since our method is cuffless, we follow the standard set by Stergiou et al. [79] to report our results. However, because this standard is relatively less informative, we also incorporate the recommendations of Stergiou et al. [78] and the BHS standard for general BP devices in our reporting.

Additionally, this study employs Bland–Altman analysis, a widely used method for assessing agreement between two measurement techniques [29]. This approach

is recommended by the Artery Society for comparing non-invasive hemodynamic measurement devices [89], offering a robust framework for evaluating the consistency and reliability of the proposed method.

Another comparison we conducted was between models with and without waveform features. Following Mukkamala et al. [55] and Mieloszyk et al., [51], we first established a baseline model without waveform features. Then, we validated the use of waveform features by measuring the increase in prediction accuracy when they were included.

Abbreviations

ARI	Adaptive reflection index
BI	Beat-to-beat interval
BP	Blood pressure
CT	Crest time
DBP	Diastolic blood pressure
DN	Dicrotic notch
DP	Diastolic peak
DT	Diastolic time
DPH	Height of the DP
EPPT	Expected PPT
ERI	Expected reflection index
ESI	Expected SI
ESP	Early systolic peak
ESPH	Height of the ESP
FP	First peak
FPH	First peak height
FFT	Fast Fourier transform
FS	Height difference between first and second peaks
HH	Heartily Happy
IP	Inflection point
IPA	Inflection point area
LP	Left peak
LV	Left valley
LSTM	Long short-term memory
MAE	Mean absolute error
MLR	Multiple linear regression
NT	Notch time
NV	Notch to valley time
PP	Pulse pressure
PPG	Photoplethysmography
PPT	Peak-to-peak time
PSD	Power spectral densities
PWA	Pulse waveform analysis
RF	Random forest
RI	Reflection index
SBP	Systolic blood pressure
SHAP	SHapley Additive exPlanations
SI	Stiffness index
SP	Second peak
SPH	Second peak height
SPS	Second peak slope
SPW-BP	Smartphone PPG-based waveform analysis for blood pressure prediction

Acknowledgements

This work was supported by the Shenzhen R & D Sustainable Development Funding [KCXFZ20230731093600002], Guangdong Digital Mental Health and Intelligent Generation Laboratory [2023WSYS010], Guangdong Philosophy and Social Science Foundation [GD23SQXY01], Shenzhen Education Science Policy Research Project [ZDZC23013], National Natural Science Foundation of China [32371121] Guangdong Science and Technology Programme [2024A0505050012], Guangdong Medical Scientific Research Foundation [B2024262] and Zhuhai City Medical Scientific Research Foundation [2420009000094].

Author contributions

IL: substantial contributions to the conception, design of the work, acquisition of data, wrote the main manuscript text FL: analysis and interpretation of data QZ: edited the manuscript NS: edited the manuscript All authors got involved in drafting the work or substantively revised, have approved the submitted version, and have agreed both to be personally accountable for the author's own contributions and to ensure that questions related to the accuracy or integrity of any

part of the work, even ones in which the author was not personally involved, are appropriately investigated, resolved, and the resolution documented in the literature.

Funding
This work was supported by the Shenzhen R & D Sustainable Development Funding [KCXFZ20230731093600002], Guangdong Digital Mental Health and Intelligent Generation Laboratory [2023WSYS010], Guangdong Philosophy and Social Science Foundation [GD23SQXY01], Shenzhen Education Science Policy Research Project [ZDZC23013], National Natural Science Foundation of China [32371121], Guangdong Science and Technology Programme [2024A0505050012], Guangdong Medical Scientific Research Foundation [B2024262] and Zhuhai City Medical Scientific Research Foundation [2420009000094].

Data availability
Data will be made available on request.

Declarations

Ethics approval and consent to participate
In accordance with the Declaration of Helsinki, this study protocol was approved by the ethical board of the corresponding author's affiliation (REC number: 201910), and informed consent was obtained from all participants.

Competing interests
The authors declare no competing interests.

Received: 25 July 2024 Accepted: 4 March 2025
Published online: 20 March 2025

References

1. Alty SR, Angarita-Jaimes N, Millasseau SC, Chowienczyk PJ. Predicting arterial stiffness from the digital volume pulse waveform. IEEE Trans Biomed Eng. 2007;54(12):2268–75.
2. Athaya T, Choi S. A review of noninvasive methodologies to estimate the blood pressure waveform. Sensors. 2022;22(10):3953.
3. Baruch MC, Warburton DE, Bredin SS, Cote A, Gerdt DW, Adkins CM. Pulse decomposition analysis of the digital arterial pulse during hemorrhage simulation. Nonlinear Biomed Phys. 2011;5(1):1–15.
4. Bashar SK, Han D, Soni A, McManus DD, Chon KH. Developing a novel noise artifact detection algorithm for smartphone PPG signals: preliminary results. IEEE EMBS Int Conf Biomed Health Inf. 2018;2018:79–82.
5. Béres S, Hejjel L. The minimal sampling frequency of the photoplethysmogram for accurate pulse rate variability parameters in healthy volunteers. Biomed Signal Process Control. 2021;68: 102589.
6. Binder S, Navratil K, Halek J. Chronic smoking and its effect on arterial stiffness. Biomed Papers Med Fac Palacky Univ Olomouc. 2008;152(2):299.
7. Bortolotto LA, Blacher J, Kondo T, Takazawa K, Safar ME. Assessment of vascular aging and atherosclerosis in hypertensive subjects: Second derivative of photoplethysmogram versus pulse wave velocity. Am J Hypertens. 2000;13(2):165–71.
8. Brown MJ. Similarities and differences between augmentation index and pulse wave velocity in the assessment of arterial stiffness. Qjm. 1999;92(10):10.
9. Cameron JD, McGrath BP, Dart AM. Use of radial artery applanation tonometry and a generalized transfer function to determine aortic pressure augmentation in subjects with treated hypertension. J Am Coll Cardiol. 1998;32(5):1214–20.
10. Chan JY-L, Leow SMH, Bea KT, Cheng WK, Phoong SW, Hong Z-W, Chen Y-L. Mitigating the multicollinearity problem and its machine learning approach: A review. Mathematics. 2022;10(8):1283.
11. Charlton PH, Celka P, Farukh B, Chowienczyk P, Alastruey J. Assessing mental stress from the photoplethysmogram: a numerical study. Physiol Meas. 2018;39(5): 054001.
12. Chowienczyk PJ, Kelly RP, MacCallum H, Millasseau SC, Andersson TL, Gosling RG, Ritter JM, Änggård EE. Photoplethysmographic assessment of pulse wave reflection: blunted response to endothelium-dependent beta2-adrenergic vasodilation in type II diabetes mellitus. Journal of the American College of Cardiology. 1999;34(7):7.
13. Christensen L, Børgesen SE. Single pulse pressure wave analysis by fast Fourier transformation. Neurol Res. 1989;11(4):197–200.
14. De Haan G, Van Leest A. Improved motion robustness of remote-PPG by using the blood volume pulse signature. Physiol Meas. 2014;35(9):1913.
15. Dey J, Gaurav A, Tiwari VN. 2018. InstaBP: cuff-less blood pressure monitoring on smartphone using single PPG sensor. 2018 40th Annual International Conference of the IEEE Engineering in Medicine and Biology Society (EMBC), 5002–5005.
16. Djeldjli D, Bousefsaf F, Maaoui C, Bereksi-Reguig F, Pruski A. Remote estimation of pulse wave features related to arterial stiffness and blood pressure using a camera. Biomed Signal Process Control. 2021;64: 102242.
17. Dormann CF, Elith J, Bacher S, Buchmann C, Carl G, Carré G, Marquéz JRG, Gruber B, Lafourcade B, Leitão PJ. Collinearity: a review of methods to deal with it and a simulation study evaluating their performance. Ecography. 2013;36(1):27–46.
18. Du Y, Wang L, Li S, Zhi G, Li D, Zhang C. Influential factors for pressure pulse waveform in healthy young adults. Biomed Mater Eng. 2015;26(s1):S497–505.

19. Elgendi M. On the analysis of fingertip photoplethysmogram signals. Curr Cardiol Rev. 2012;8(1):14–25.
20. Elgendi M, Norton I, Brearley M, Abbott D, Schuurmans D. Detection of a and b waves in the acceleration photoplethysmogram. Biomed Eng Online. 2014;13(1):1–18.
21. El-Hajj C, Kyriacou PA. A review of machine learning techniques in photoplethysmography for the non-invasive cuffless measurement of blood pressure. Biomed Signal Process Control. 2020;58: 101870.
22. Eom H, Lee D, Han S, Hariyani YS, Lim Y, Sohn I, Park K, Park C. End-to-end deep learning architecture for continuous blood pressure estimation using attention mechanism. Sensors. 2020;20(8):2338.
23. Fine J, Branan KL, Rodriguez AJ, Boonya-Ananta T, Ramella-Roman JC, McShane MJ, Coté GL. Sources of inaccuracy in photoplethysmography for continuous cardiovascular monitoring. Biosensors. 2021;11(4):126.
24. Forouzanfar M, Dajani HR, Groza VZ, Bolic M, Rajan S, Batkin I. Oscillometric blood pressure estimation: Past, present, and future. IEEE Rev Biomed Eng. 2015;8:44–63.
25. Frey L, Menon C, Elgendi M. Blood pressure measurement using only a smartphone. Npj Dig Med. 2022;5(1):1. https://doi.org/10.1038/s41746-022-00629-2.
26. Fujime M, Tomimatsu T, Okaue Y, Koyama S, Kanagawa T, Taniguchi T, Kimura T. Central aortic blood pressure and augmentation index during normal pregnancy. Hypertens Res. 2012;35(6):633–8. https://doi.org/10.1038/hr.2012.1.
27. Gao SC, Wittek P, Zhao L, Jiang WJ. 2016. Data-driven estimation of blood pressure using photoplethysmographic signals. 2016 38th annual international conference of the IEEE engineering in medicine and biology society (EMBC), 766–769.
28. Gaurav A, Maheedhar M, Tiwari VN, Narayanan R. 2016. Cuff-less PPG based continuous blood pressure monitoring—a smartphone based approach. 2016 38th Annual International Conference of the IEEE Engineering in Medicine and Biology Society (EMBC), 607–610.
29. Giavarina D. Understanding bland Altman analysis. Biochemia Medica. 2015;25(2):141–51.
30. Halsey LG. The reign of the p-value is over: What alternative analyses could we employ to fill the power vacuum? Biol Let. 2019;15(5):20190174.
31. Haugg F, Elgendi M, Menon C. Assessment of blood pressure using only a smartphone and machine learning techniques: a systematic review. Front Cardiovas Med. 2022;9: 894224.
32. Hsu Y-C, Li Y-H, Chang C-C, Harfiya LN. Generalized deep neural network model for cuffless blood pressure estimation with photoplethysmogram signal only. Sensors. 2020;20(19):5668.
33. IEEE. 2014. 1708–2014—IEEE standard for wearable cuffless blood pressure measuring devices. https://ieeexplore.ieee.org/document/6882122
34. IEEE. 2019. 1708a-2019—IEEE standard for wearable, cuffless blood pressure measuring devices—amendment 1.
35. ISO. 2022. ISO 81060–3:2022 Non-invasive sphygmomanometers part 3: clinical investigation of continuous automated measurement type. https://www.iso.org/standard/71161.html
36. Jonathan E, Leahy MJ. Cellular phone-based photoplethysmographic imaging. J Biophoton. 2011;4(5):5.
37. Katsanos AH, Filippatou A, Manios E, Deftereos S, Parissis J, Frogoudaki A, Vrettou A-R, Ikonomidis I, Pikilidou M, Kargiotis O, Voumvourakis K, Alexandrov AW, Alexandrov AV, Tsivgoulis G. Blood pressure reduction and secondary stroke prevention: a systematic review and metaregression analysis of randomized clinical trials. Hypertension. 2017;69(1):171–9. https://doi.org/10.1161/HYPERTENSIONAHA.116.08485.
38. Kelly RP, Millasseau SC, Ritter JM, Chowienczyk PJ. Vasoactive drugs influence aortic augmentation index independently of pulse-wave velocity in healthy men. Hypertension. 2001;37(6):1429–33.
39. Khanoka B, Slovik Y, Landau D, Nitzan M. Sympathetically induced spontaneous fluctuations of the photoplethysmographic signal. Med Biol Eng Compu. 2004;42(1):80–5. https://doi.org/10.1007/BF02351014.
40. Kim G, Kim J-H, Moon K-W, Yoo K-D, Ihm S-H, Youn H-J, Kim C-M. The clinical usefulness of central hemodynamics to evaluate diastolic dysfunction in subjects without hypertension. Clin Interv Aging. 2014;9:527.
41. Korpas D, Halek J, Doležal L. Parameters describing the pulse wave. Physiol Res. 2009;58(4):473.
42. Lee J, Matsumura K, Yamakoshi K, Rolfe P, Tanaka S, Yamakoshi T. 2013. Comparison between red, green and blue light reflection photoplethysmography for heart rate monitoring during motion. 2013 35th Annual International Conference of the IEEE Engineering in Medicine and Biology Society (EMBC), 1724–1727. https://ieeexplore.ieee.org/abstract/document/6609852/
43. Liu I, Liu F, Zhong Q, Ma F, Ni S. Your blush gives you away: detecting hidden mental states with remote photoplethysmography and thermal imaging. PeerJ Computer Science. 2024;10: e1912.
44. Liu I, Ni S, Peng K. Enhancing the robustness of smartphone photoplethysmography: a signal quality index approach. Sensors. 2020;20(7):1923.
45. London AJ. Artificial intelligence and black-box medical decisions: accuracy versus explainability. Hastings Cent Rep. 2019;49(1):15–21.
46. Longmore SK, Lui GY, Naik G, Breen PP, Jalaludin B, Gargiulo GD. A comparison of reflective photoplethysmography for detection of heart rate, blood oxygen saturation, and respiration rate at various anatomical locations. Sensors. 2019;19(8):1874.
47. Lundberg SM, Lee S-I. A unified approach to interpreting model predictions. Adv Neural Inf Proc Syst. 2017;30:1.
48. Maeda Y, Sekine M, Tamura T. The advantages of wearable green reflected photoplethysmography. J Med Syst. 2011;35(5):829–34. https://doi.org/10.1007/s10916-010-9506-z.
49. Martínez CAG, Quintana AO, Vila XA, Touriño MJL, Rodríguez-Liñares L, Presedo JMR, Penín AJM. Heart rate variability analysis with the R package RHRV. Berlin: Springer; 2017.
50. Melenovsky V, Borlaug BA, Fetics B, Kessler K, Shively L, Kass DA. Estimation of central pressure augmentation using automated radial artery tonometry. J Hypertens. 2007;25(7):1403–9.
51. Mieloszyk R, Twede H, Lester J, Wander J, Basu S, Cohn G, Smith G, Morris D, Gupta S, Tan D. A comparison of wearable tonometry, photoplethysmography, and electrocardiography for cuffless measurement of blood pressure in an ambulatory setting. IEEE J Biomed Health Inform. 2022;26(7):2864–75.
52. Millasseau SC, Kelly RP, Ritter JM, Chowienczyk PJ. Determination of age-related increases in large artery stiffness by digital pulse contour analysis. Clin Sci. 2002;103(4):371–7.

53. Millasseau SC, Ritter JM, Takazawa K, Chowienczyk PJ. Contour analysis of the photoplethysmographic pulse measured at the finger. J Hypertens. 2006;24(8):1449–56.
54. Molnar C, Casalicchio G, Bischl B. Interpretable machine learning–a brief history, state-of-the-art and challenges. Joint European conference on machine learning and knowledge discovery in databases, 2020; 417–431.
55. Mukkamala R, Shroff SG, Landry C, Kyriakoulis KG, Avolio AP, Stergiou GS. The microsoft research aurora project: important findings on cuffless blood pressure measurement. Hypertension. 2023;80(3):534–40. https://doi.org/10.1161/HYPERTENSIONAHA.122.20410.
56. Murdoch WJ, Singh C, Kumbier K, Abbasi-Asl R, Yu B. Definitions, methods, and applications in interpretable machine learning. Proc Natl Acad Sci. 2019;116(44):22071–80.
57. Murtaugh PA. In Defense of p values. Ecology. 2014;95(3):611–7.
58. Nam Y, Nam Y-C. Photoplethysmography signal analysis for optimal region-of-interest determination in video imaging on a built-in smartphone under different conditions. Sensors. 2017;17(10):2385.
59. Nemcova A, Jordanova I, Varecka M, Smisek R, Marsanova L, Smital L, Vitek M. Monitoring of heart rate, blood oxygen saturation, and blood pressure using a smartphone. Biomed Signal Process Control. 2020;59: 101928.
60. Nichols WW, Denardo SJ, Wilkinson IB, McEniery CM, Cockcroft J, O'Rourke MF. Effects of arterial stiffness, pulse wave velocity, and wave reflections on the central aortic pressure waveform. J Clin Hypertension. 2008;10(4):295–303. https://doi.org/10.1111/j.1751-7176.2008.04746.x.
61. O'Brien E. Demise of the mercury sphygmomanometer and the dawning of a new era in blood pressure measurement. Blood Press Monit. 2003;8(1):19–21.
62. O'Brien E, Petrie J, Littler W, De Swiet M, Padfield PL, Altman D, Bland M, Coats A, Atkins N. The British hypertension society protocol for the evaluation of blood pressure measuring devices. J Hypertens. 1993;11(Suppl 2):S43–62.
63. O'Rourke MF, Pauca A, Jiang X-J. Pulse wave analysis. Br J Clin Pharmacol. 2001;51(6):507–22.
64. Padilla JM, Berjano EJ, Saiz J, Facila L, Diaz P, Merce S. Assessment of relationships between blood pressure, pulse wave velocity and digital volume pulse. Comput Cardiol. 2006;2006:893–6.
65. Panula T, Blomster J, Pänkäälä M, Koivisto T, Kaisti M. An automated device for recording peripheral arterial waveform. 2019 Computing in Cardiology (CinC), 2019; 1–4.
66. Park JW, Evans HI, Watson H, Abowd GD, Arriaga RI. Growing apart: how smart devices impact the proximity of users to their smartphones. IEEE Pervasive Comput. 2020;19(3):79–88.
67. Pauca AL, O'Rourke MF, Kon ND. Prospective evaluation of a method for estimating ascending aortic pressure from the radial artery pressure waveform. Hypertension. 2001;38(4):932–7. https://doi.org/10.1161/hy1001.096106.
68. Peltokangas M, Vehkaoja A, Verho J, Huotari M, Röning J, Lekkala J. Monitoring arterial pulse waves with synchronous body sensor network. IEEE J Biomed Health Inf. 2014;18(6):6.
69. Peng R-C, Zhou X-L, Lin W-H, Zhang Y-T. Extraction of heart rate variability from smartphone photoplethysmograms. Comput Math Methods Med. 2015;1:1–11.
70. Poon, C. C. Y., & Zhang, Y. T. (2006). Cuff-less and noninvasive measurements of arterial blood pressure by pulse transit time. 2005 IEEE Engineering in Medicine and Biology 27th annual conference, 5877–5880.
71. Qin C, Li Y, Liu C, Ma X. Cuff-less blood pressure prediction based on photoplethysmography and modified ResNet. Bioengineering. 2023;10(4):400.
72. Radha M, De Groot K, Rajani N, Wong CC, Kobold N, Vos V, Fonseca P, Mastellos N, Wark PA, Velthoven N. Estimating blood pressure trends and the nocturnal dip from photoplethysmography. Physiol Meas. 2019;40(2): 025006.
73. Schutte AE, Kollias A, Stergiou GS. Blood pressure and its variability: classic and novel measurement techniques. Nat Rev Cardiol. 2022;19(10):643–54.
74. Sharma A, Tanwar RS, Singh Y, Sharma A, Daudra S, Singal G, Gadekallu TR, Pancholi S. Heart rate and blood pressure measurement based on photoplethysmogram signal using fast Fourier transform. Comput Electr Eng. 2022;101: 108057.
75. Sharman JE, McEniery CM, Campbell RI, Coombes JS, Wilkinson IB, Cockcroft JR. The effect of exercise on large artery haemodynamics in healthy young men. Eur J Clin Invest. 2005;35(12):738–44.
76. Simek J, Wichterle D, Melenovský V, Malík J, Svacina S, Widimský J. Second derivative of the finger arterial pressure waveform: an insight into dynamics of the peripheral arterial pressure pulse. Physiol Res. 2005;54(5):505–13.
77. Steinman J, Barszczyk A, Sun H-S, Lee K, Feng Z-P. Smartphones and video cameras: future methods for blood pressure measurement. Front Dig Health. 2021;3: 770096.
78. Stergiou GS, Alpert B, Mieke S, Asmar R, Atkins N, Eckert S, Frick G, Friedman B, Graßl T, Ichikawa T. A universal standard for the validation of blood pressure measuring devices: association for the advancement of medical instrumentation/European society of hypertension/international organization for standardization (AAMI/ESH/ISO) collaboration statement. Hypertension. 2018;71(3):368–74.
79. Stergiou GS, Mukkamala R, Avolio A, Kyriakoulis KG, Mieke S, Murray A, Parati G, Schutte AE, Sharman JE, Asmar R. Cuffless blood pressure measuring devices: Review and statement by the European society of hypertension working group on blood pressure monitoring and cardiovascular variability. J Hypertens. 2022;40(8):1449–60.
80. Laborde S, Mosley E, Thayer JF. Heart rate variability and cardiac vagal tone in psychophysiological research—recommendations for experiment planning, data analysis, and data reporting. Front Psychol. 2017. https://doi.org/10.3389/fpsyg.2017.00213.
81. Tabei F, Gresham JM, Askarian B, Jung K, Chong JW. Cuff-less blood pressure monitoring system using smartphones. IEEE Access. 2020;8:11534–45.
82. Takazawa K, Tanaka N, Fujita M, Matsuoka O, Saiki T, Aikawa M, Tamura S, Ibukiyama C. Assessment of vasoactive agents and vascular aging by the second derivative of photoplethysmogram waveform. Hypertension. 1998;32(2):365–70.
83. Tanveer MS, Hasan MK. Cuffless blood pressure estimation from electrocardiogram and photoplethysmogram using waveform based ANN-LSTM network. Biomed Signal Process Control. 2019;51:382–92.
84. Teng XF, Zhang YT. Continuous and noninvasive estimation of arterial blood pressure using a photoplethysmographic approach. Proceedings of the 25th Annual International Conference of the IEEE Engineering in Medicine and Biology Society (IEEE Cat. No. 03CH37439), 4, 3153–3156. 2003.

85. Vellido A. The importance of interpretability and visualization in machine learning for applications in medicine and health care. Neural Comput Appl, 2019; 1–15.
86. Venables WN, Ripley BD. Modern applied statistics with S-PLUS. Berlin: Springer Science & Business Media; 2013.
87. Wang C, Li X, Hu H, Zhang L, Huang Z, Lin M, Zhang Z, Yin Z, Huang B, Gong H, Bhaskaran S, Gu Y, Makihata M, Guo Y, Lei Y, Chen Y, Wang C, Li Y, Zhang T, Xu S. Monitoring of the central blood pressure waveform via a conformal ultrasonic device. Nat Biomed Eng. 2018;2(9):687–95. https://doi.org/10.1038/s41551-018-0287-x.
88. Wang L, Pickwell-MacPherson E, Liang YP, Zhang YT. Noninvasive cardiac output estimation using a novel photoplethysmogram index. Ann Int Conf IEEE Eng Med Biol Soc. 2009;2009:1746–9.
89. Wilkinson IB, McEniery CM, Schillaci G, Boutouyrie P, Segers P, Donald A, Chowienczyk PJ. ARTERY Society guidelines for validation of non-invasive haemodynamic measurement devices: part 1, arterial pulse wave velocity. Artery Res. 2010;4(2):34–40.
90. Xiao H, Tan I, Butlin M, Li D, Avolio AP. Mechanism underlying the heart rate dependency of wave reflection in the aorta: a numerical simulation. Am J Physiol-Heart Circ Physiol. 2018;314(3):3.
91. Yoon Y-H, Kim J, Lee KJ, Cho D, Oh JK, Kim M, Roh J-H, Park HW, Lee J-H. Blood pressure measurement based on the camera and inertial measurement unit of a smartphone: instrument validation study. JMIR Mhealth Uhealth. 2023;11(1): e44147.

Publisher's Note